Chinese Journal of Aeronautics, (2014),27(2): 338–348

Chinese Society of Aeronautics and Astronautics
& Beihang University

Chinese Journal of Aeronautics

cja@buaa.edu.cn
www.sciencedirect.com

Fast low-energy halo-to-halo transfers between Sun–planet systems

Shang Haibin, Wang Shuai *, Cui Pingyuan

Key Laboratory of Dynamics and Control of Flight Vehicle, Ministry of Education, Beijing Institute of Technology, Beijing 100081, China

Received 24 April 2013; revised 9 August 2013; accepted 14 October 2013
Available online 20 February 2014

KEYWORDS

Astrophysics;
Halo orbit;
Low-energy;
Planetary gravity assist;
Pseudo-manifold

Abstract In this paper, the problem of fast low-energy halo-to-halo transfers between Sun–planet systems is discussed under ephemeris constraints. According to the structure of an invariant manifold, employing an invariant manifold and planetary gravity assist to save fuel consumption is analyzed from the view of orbital energy. Then, a pseudo-manifold is introduced to replace the invariant manifold in such a way that more transfer opportunities are allowed. Fast escape and capture can be achieved along the pseudo-manifold. Furthermore, a global searching method that is based on patched-models is proposed to find an appropriate transfer trajectory. In this searching method, the trajectory is divided into several segments that can be designed under simple dynamical models, and an analytical algorithm is developed for connecting the segments. Earth–Mars and Earth–Venus halo-to-halo transfers are designed to demonstrate the proposed approach. Numerical results show that the transfers that combine the pseudo-manifolds and planetary gravity assist can offer significant fuel consumption and flight time savings over traditional transfer schemes.

1. Introduction

Halo orbit is one of the complex motions that are near to the equilibrium point of a three-body system. The specific position and dynamic characteristics of a halo orbit lead to a significant application value in space exploration missions.[1–4] One of these applications is to use a halo orbit as a transfer station for a deep space exploration mission.[5,6] This approach leads to a new research hotspot that involves how to transfer a spacecraft between halo orbits of different Sun–planet systems.

A common method for designing a transfer between halo orbits of different Sun–planet systems is connecting an unstable manifold and a stable manifold in deep space under a heliocentric two-body model.[7–10] There are two issues in this transfer scheme: (1) the flying time along the traditional invariant manifold is usually very long, for example, the flying time for an Earth–Venus halo-to-halo transfer with minimum fuel consumption is approximately three years;[8] and (2) only low fuel consumption savings can be offered.[11] Thus, constructing a transfer with less fuel consumption and a shorter flying time is a problem that is worthwhile studying. Nakamiya et al. suggested a transfer scheme that combined an invariant manifold with planetary gravity assist.[12] This transfer scheme can

* Corresponding author. Tel.: +86 10 68918921.
E-mail addresses: shanghb@bit.edu.cn (H. Shang), bitwangshuai@gmail.com (S. Wang), cuipy@bit.edu.cn (P. Cui).

Peer review under responsibility of Editorial Committe of CJA.

1000-9361 © 2014 Production and hosting by Elsevier Ltd. on behalf of CSAA & BUAA. Open access under CC BY-NC-ND license.
http://dx.doi.org/10.1016/j.cja.2014.02.005

achieve a significant amount of fuel consumption savings due to the introduction of planetary gravity assist. However, there is a lack of a systematic methodology to design the trajectory of this transfer scheme. In this paper, in-depth research is conducted to solve this problem.

For a halo-to-halo transfer between Sun–planet systems, a fast low-energy transfer scheme is analyzed, and a novel global searching method is proposed under ephemeris constraints. Firstly, a transfer scheme that combines an invariant manifold and planetary gravity-assist is analyzed. Then, a pseudo-manifold is introduced and analyzed. When employing a pseudo-manifold instead of an invariant manifold, more transfer opportunities are allowed and a shorter flying time is needed. Furthermore, a fast global searching method based on patched-models is proposed. Finally, the proposed approach is validated by using numerical simulations to design Earth–Mars and Earth–Venus halo-to-halo transfers.

2. Problem statement

In a halo-to-halo transfer between Sun–planet systems, the motion of a spacecraft is influenced mainly by the gravitation of three celestial bodies: Sun, the escape planet, and the capture planet. Based on the dynamic characteristics, the whole trajectory is divided into several segments in this paper, and each segment is described with a simple dynamic model that has few errors.

The motion around the planet is researched mainly under the circular restricted three-body model. In the circular restricted three-body problem (CRTBP) shown in Fig. 1, the motion of the spacecraft P_3 is studied in the gravitational field that is generated by two primaries, $P_1(m_1)$ and $P_2(m_2)$. The two primaries rotate about their common center of mass in a circular motion.

To investigate the motion of P_3, the rotating coordinate $oxyz$ is defined as follows: the origin is at the center of mass, the x-axis is directed to P_2, the y-axis is directed to the velocity of P_2, and the z-axis completes the right-hand coordinate frame. With non-dimensional units: the unit mass M^* is the sum of the two primaries, the unit length L^* is the distance between them, and the unit time T^* is $1/(2\pi)$ of the primary's moving periodic. Here, $\mu = m_2/(m_1 + m_2)$ is the mass parameter, and the motion equations of the spacecraft are[13]

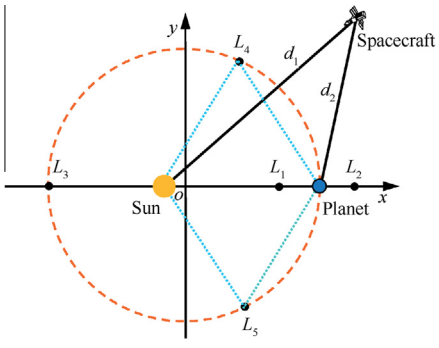

Fig. 1 Circular restricted three-body problem.

$$\begin{cases} \ddot{x} - 2\dot{y} = \frac{\partial \Omega}{\partial x} \\ \ddot{y} + 2\dot{x} = \frac{\partial \Omega}{\partial y} \\ \ddot{z} = \frac{\partial \Omega}{\partial z} \end{cases} \tag{1}$$

where the potential of the system is

$$\Omega = \frac{x^2 + y^2 + z^2}{2} + \frac{1-\mu}{d_1} + \frac{\mu}{d_2} + \frac{\mu(1-\mu)}{2} \tag{2}$$

and d_1 and d_2 are the distances between the spacecraft and the two primaries, respectively.

The energy of P_3 is presented by the Jacobi integral constant as

$$C = 2\Omega - (\dot{x}^2 + \dot{y}^2 + \dot{z}^2) \tag{3}$$

The restricted three-body problem has five well-known equilibrium points. Three collinear points lie on the x-axis and are called L_1, L_2, and L_3, and there are two equilateral points which are called L_4 and L_5, as shown in Fig. 1. Because of the saddle–center–center type of the collinear equilibrium points, periodical motion and hyperbolical motion exist around these three equilibrium points.[14] The periodical motion allows the existence of periodic orbits known as halo orbits. The halo orbits can be found by employing an analytical approach and a differential correction strategy.[15] The hyperbolical motion allows the existence of ballistic trajectories that move to/from these periodic orbits asymptotically. These trajectories are known as stable/unstable manifolds of the periodic orbits.

In this paper, we focus on the halo orbits around the two collinear points L_1 and L_2. To calculate the manifolds of a halo orbit,[16] the reference point $\boldsymbol{X}_0 = \boldsymbol{X}(t_r)$ on the periodic orbit is selected. Then, the non-dimensional parameter $\tau \in [0, 1]$ is defined to indicate the time between any point on the periodic orbit and the reference point:

$$t_\tau = t_r + \tau T_H \tag{4}$$

where T_H is the period of the halo orbit.

By calculating the eigenvalues and eigenvectors of the monodromy matrix $\boldsymbol{M}(\tau = 1, t_r)$, the stable eigenvector $\boldsymbol{\eta}^S$ and the unstable eigenvector $\boldsymbol{\eta}^U$ on the reference point are obtained. The stable and unstable eigenvectors on the other points of the halo orbit can be calculated by

$$\begin{cases} \boldsymbol{\eta}^S(\boldsymbol{X}(\tau)) = \boldsymbol{M}(\tau, t_r)\boldsymbol{\eta}^S(\boldsymbol{X}_0) \\ \boldsymbol{\eta}^U(\boldsymbol{X}(\tau)) = \boldsymbol{M}(\tau, t_r)\boldsymbol{\eta}^U(\boldsymbol{X}_0) \end{cases} \tag{5}$$

where $\boldsymbol{M}(\tau, t_r)$ is the state transition matrix between $\boldsymbol{X}(t_r)$ and $\boldsymbol{X}(\tau)$.

If the perturbation is performed in the direction of the unstable eigenvector $\boldsymbol{\eta}^U$/stable eigenvector $\boldsymbol{\eta}^S$, the particle on the halo orbit will asymptotically depart from the halo orbit as the time flows forward/backward. Furthermore, the initial states of the manifolds on the halo orbit can be calculated by

$$\begin{cases} \boldsymbol{X}^{S\pm}(\boldsymbol{X}(\tau)) = \boldsymbol{X}(\tau) \pm \varepsilon \frac{\boldsymbol{\eta}^S(\boldsymbol{X}(\tau))}{\|\boldsymbol{\eta}^S(\boldsymbol{X}(\tau))\|} \\ \boldsymbol{X}^{U\pm}(\boldsymbol{X}(\tau)) = \boldsymbol{X}(\tau) \pm \varepsilon \frac{\boldsymbol{\eta}^U(\boldsymbol{X}(\tau))}{\|\boldsymbol{\eta}^U(\boldsymbol{X}(\tau))\|} \end{cases} \tag{6}$$

where ε is a small value that is commonly chosen to make the position perturbation within the range of 20–50 km.[17]

By integrating the states that are obtained from Eq. (6), the invariant manifolds of Sun–Earth are obtained and drawn in Fig. 2. In the figure, W indicates the set of manifolds, and

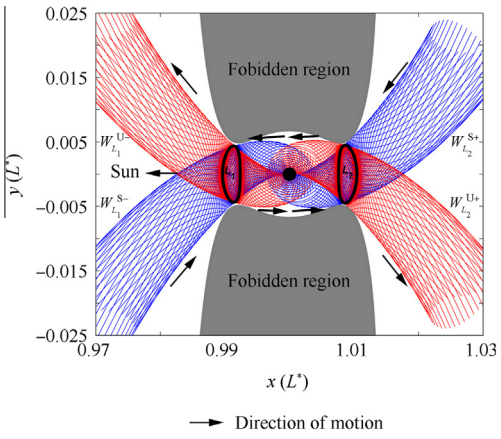

Fig. 2 Planar views of the invariant manifolds correspond to halo orbits of the Sun–Earth system.

the superscripts "U" and "S" indicate the manifolds that are unstable and stable, the superscripts "+" and "−" indicate the manifolds that are on the right and left sides, respectively. It can be seen that there exist four invariant manifold sets that are associated with each halo orbit, among which two are on the left side and the other two are on the right side. On each side, one set comprises stable manifolds and the other set comprises unstable manifolds.

Based on the properties of an invariant manifold, an unstable/stable manifold can be taken as an escape/capture trajectory. In the remainder of this article, we will use an escape trajectory as an example to explain which set of manifolds is more suitable to use in the transfer. For the invariant manifolds of a given halo orbit, the Jacobi constants C_H are constant. To achieve a transfer that aims at the target halo orbit, at least one impulse must be performed on the spacecraft to allow the spacecraft to enter into an interplanetary trajectory whose Jacobi constant is C_T. The variation of the Jacobi constant is

$$\Delta C = C_H - C_T \tag{7}$$

It can be seen from Eq. (3) that the Jacobi constant is composed of the potential energy and the kinetic energy. For a Sun–planet system, the mass parameter μ is so small that the distances between the manifolds and the Sun are almost the same. Thus, the first two items of the potential are insensitive to the variation in the spacecraft position on the manifolds. Therefore, the potential of the spacecraft on the L_1 and L_2 invariant manifolds can be approximated as

$$\Omega \approx 1.5 + \mu/d_2 \tag{8}$$

For different sets of invariant manifolds, the differences in the values of the ratio μ/d_2 are quite large. More specifically, this item varies dramatically near the planet. Because the Jacobi constant remains unchanged on the invariant manifolds, the velocity and the change efficiency of the energy are larger when the spacecraft is near to the planet. Therefore, employing the unstable/stable manifolds directed to the planet and proposing the impulse around the planet could lower fuel consumption. The principle of this transfer scheme is that the trajectory employs the gravitational effect of the planet to save on the fuel consumption cost.

The schematic diagram of the transfer scheme is shown in Fig. 3. In this transfer scheme, the spacecraft first approaches the initial planet asymptotically along an unstable manifold that corresponds to the initial halo orbit, and flies to the target planet with an impulse $\Delta \boldsymbol{v}_D$ performed around the escape planet. Then, it enters into a stable manifold around the target planet by the execution of an impulse $\Delta \boldsymbol{v}_A$. Later, it asymptotically approaches the target halo orbit along its stable manifold. According to the characteristics of this transfer scheme, the whole trajectory is divided into five segments as follows: unstable manifold segment, escape segment, interplanetary segment, capture segment, and stable manifold segment. In the following, we will focus on investigating the characteristics and the design method of this transfer scheme.

3. Pseudo-manifold

For the interplanetary transfer mission design, not only the fuel consumption but also the flying time should be considered. Typically, following an invariant manifold from a halo orbit to the vicinity of a planet takes a very long time. A large amount of time is wasted when increasing the perturbation around the halo orbit. The flying time around the halo orbit depends on the stability of the perturbed point on the halo orbit. The manifold can arrive at the vicinity of the planet more quickly as the stability becomes more weak.[18] It is also known that the stability of a perturbed point can be reduced by increasing the

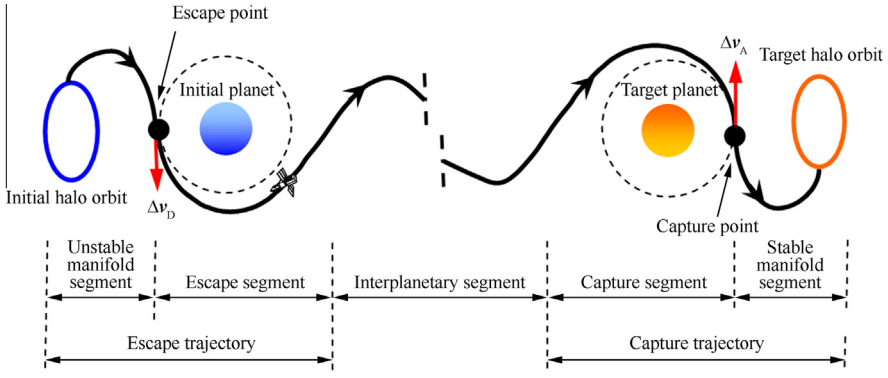

Fig. 3 Phases of a halo-to-halo transfer that employs invariant manifolds and planetary gravity assist.

perturbation. Therefore, when an appropriate large perturbation is proposed, the spacecraft can depart or approach the halo orbit quickly. In this paper, the concept of the pseudo-manifold is introduced to design a fast low-energy interplanetary transfer trajectory. The pseudo-manifold considered in this paper contains the following characteristics: (1) perturbation is applied only on the velocity; (2) the direction of the perturbation is the same as that of the stable and unstable eigenvectors; and (3) the value of the perturbed velocity is in the range of 1.0×10^{-5}–3.0×10^{-1} km/s. The initial velocity of the perturbed point on the pseudo-manifold can be written as

$$\begin{cases} \boldsymbol{V}^{\mathrm{S}\pm} = \boldsymbol{V}_0 \pm \Delta V \boldsymbol{\chi}^{\mathrm{S}} \\ \boldsymbol{V}^{\mathrm{U}\pm} = \boldsymbol{V}_0 \pm \Delta V \boldsymbol{\chi}^{\mathrm{U}} \end{cases} \tag{9}$$

where ΔV is the value of the perturbed velocity, $\boldsymbol{V}_0$ the original velocity, and $\boldsymbol{\chi}^{\mathrm{S}}$ and $\boldsymbol{\chi}^{\mathrm{U}}$ are the velocity components of the unit stable and unstable eigenvectors, respectively. $\boldsymbol{\chi}^{\mathrm{S}}$ (or $\boldsymbol{\chi}^{\mathrm{U}}$) is parallel to the vector that is composed of the last three elements of $\boldsymbol{\eta}^{\mathrm{U}}$ (or $\boldsymbol{\eta}^{\mathrm{S}}$), and its value is unit.

In Fig. 4, the pseudo-manifolds of the Sun–Earth L_1 northern halo orbit are drawn. The amplitude of the halo orbit in the z direction is 1.6×10^5 km, and the perturbed velocity is equal to ΔV = 100 m/s. And the superscripts "PU" and "PS" indicate the pseudo-manifolds that are unstable and stable. It can be seen that the pseudo-manifolds have the same evolutionary trend as traditional invariant manifolds.

To investigate the influence of the perturbed velocity on the flying time, the Poincare map with the constraint $x = 1-\mu$ is created. The flying time from the halo orbit to the Poincare map along the pseudo-manifolds is drawn in Fig. 5. t indicates the departure position through the departure time, and the t_s represents the flying time. Fig. 5 shows that the flying time is approximately 200 days for the invariant manifolds, while the shortest flying time is only 73.79 days for the pseudo-manifolds with ΔV = 50 m/s and 37.98 days for the pseudo-manifolds with ΔV = 300 m/s. In general, the flying time can be reduced substantially, which results in lower fuel consumption.

As mentioned above, with an impulse, the energy changes more efficiently as the velocity increases. For a given manifold branch, the velocity at the periapsis related to the planet is a local maximum. Thus, the impulse is chosen to be performed at the periapsis. The position of the spacecraft relative to the

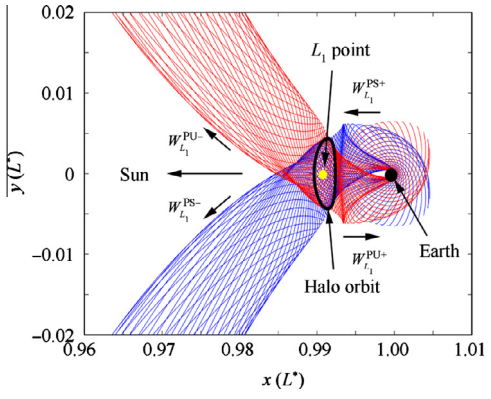

Fig. 4 Pseudo-manifolds of the Sun–Earth L_1 halo orbit.

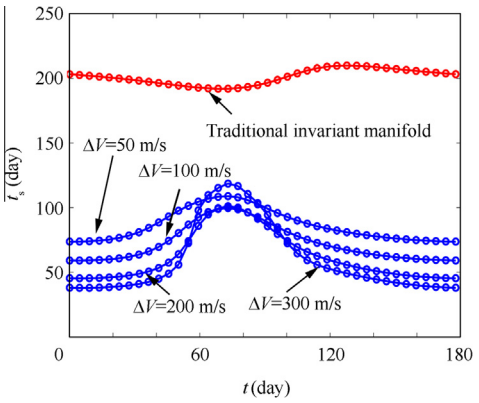

Fig. 5 Flying time for the manifolds arriving at the Poincare map.

planet is defined as $\boldsymbol{\xi} = [x-1+\mu\ y\ z]^T$. The periapsis Poincare map should satisfy the following constraints:[19]

$$\begin{cases} \boldsymbol{\xi}^{\mathrm{T}}\dot{\boldsymbol{\xi}} = 0 \\ \dot{\boldsymbol{\xi}}^{\mathrm{T}}\dot{\boldsymbol{\xi}} + \boldsymbol{\xi}^{\mathrm{T}}\ddot{\boldsymbol{\xi}} \geqslant 0 \end{cases} \tag{10}$$

The periapsides of the pseudo-manifolds can be obtained by integrating the perturbed points until arriving at the periapsis Poincare map. The projections of the Sun–Earth L_1 and L_2 pseudo-manifolds on the periapsis Poincare map are drawn in Fig. 6, in which the perturbed velocity is 100 m/s.

It can be seen from Fig. 6 that the periapsides of the L_1 pseudo-manifolds are symmetrical with those of the L_2 pseudo-manifolds about Earth. The periapsides are mainly located in the region where the distance to Earth is shorter than 7.5×10^5 km, and many of them are very near to Earth. These make it possible to achieve low-energy transfers by employing the pseudo-manifolds. It should be noted that only the periapsides around Earth are drawn in Fig. 6. The periapsides that are far away from Earth are not fit for transferring when viewed from the perspective of planetary gravity assist. Therefore, to reduce unnecessary computational consumption, the Poincare map is further constrained by

$$r_{\mathrm{P}} < \|\boldsymbol{\xi}\| \leqslant r_{\max} \tag{11}$$

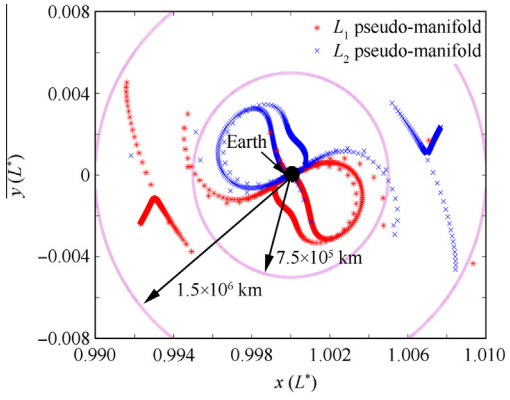

Fig. 6 Projections of the Sun–Earth L_1 and L_2 pseudo-manifolds on the periapsis Poincare map.

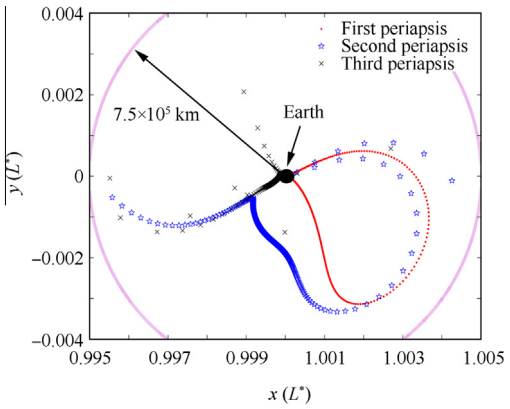

Fig. 7 Projections of the L_1 pseudo-manifolds on the periapsis Poincare map.

where r_P is the safe distance, which is slightly longer than the radius of the planet, and r_{max} the allowable maximum value of the distance to the planet.

The projections of the L_1 pseudo-manifolds ($\Delta V = 100$ m/s) on the periapsis Poincare map are drawn in Fig. 7. The time for the L_1 pseudo-manifolds arriving at the periapsis Poincare map is shown in Fig. 8. The orders of a manifold trajectory's periapsides are distinguished by differently shaped points.

Fig. 7 shows that, near to Earth, many of the points are in the first and third periapsides, and the first periapsides constitute a continuous closed curve. Among each set of the periapsides of the same order, the appropriate transfer opportunities can be found. However, the first periapsides usually cost less time. It can be seen from Fig. 8 that the time for the pseudo-manifolds to arrive at the first periapsides is less than 100 days and varies reposefully, while the time for the other periapsides is longer and varies acutely. Moreover, the first periapsides are all in the region where the distance to Earth is shorter than 7.5×10^5 km, while lots of the second and third periapsides are outside of this region. Therefore, only the first periapsides are considered in the transfer trajectory design.

To investigate the influence of the perturbed velocity ΔV on the periapsis distribution, the projections of the pseudo-manifold periapsides on different planes are drawn in Fig. 9.

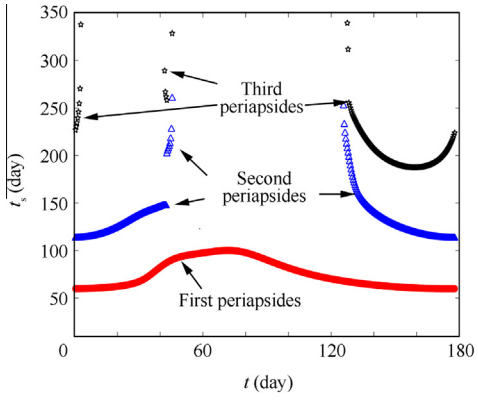

Fig. 8 Time for the L_1 pseudo-manifolds arriving at the periapsis Poincare map.

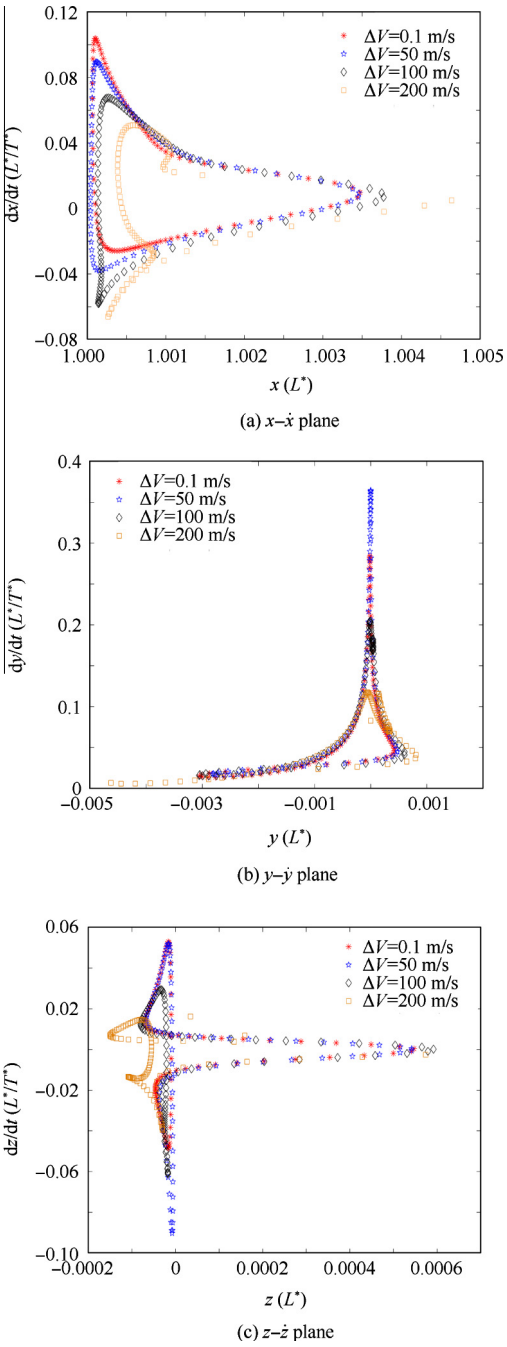

Fig. 9 Projections of the pseudo-manifold periapsides on the $x - \dot{x}, y - \dot{y}$ and $z - \dot{z}$ planes.

As shown in Fig. 9, the distributions of the pseudo-manifold periapsides are very similar in the phase space, especially for $\Delta V < 100$ m/s. When ΔV is equal to 200 m/s, the projections of the periapsides change greatly. While considering the influence of the perturbed velocity on the flying time shown in Fig. 5, the following conclusions can be obtained: the lower the perturbed velocity ΔV is, the stronger the influence of ΔV on the flying time is; furthermore, the influence of ΔV on states of periapsides is stronger when ΔV is higher. It follows that the pseudo-manifolds can not only save flying time but also expand transfer opportunities.

4. Transfer trajectory design

4.1. Trajectory searching method

On the basis of the discussion above, for a given halo-to-halo transfer between Sun–planet systems, the design parameters of a transfer trajectory that employs pseudo-manifolds and planetary gravity assist are

$$\boldsymbol{Z} = \left[\boldsymbol{t}_0 \quad t_{\mathrm{I}} \quad \tau_{\mathrm{D}} \quad \tau_{\mathrm{A}} \quad \Delta V_{\mathrm{D}} \quad \Delta V_{\mathrm{A}} \quad \Delta \boldsymbol{v}_{\mathrm{D}}^{\mathrm{T}} \quad \Delta \boldsymbol{v}_{\mathrm{A}}^{\mathrm{T}}\right]^{\mathrm{T}} \tag{12}$$

where t_0 is the moment when the spacecraft departs the initial halo orbit, t_{I} the time from the escape point to the capture point, $\tau_{\mathrm{D}} \in [0, 1]$ and $\tau_{\mathrm{A}} \in [0, 1]$ indicate the phases on the initial and final halo orbits, ΔV_{D} is the perturbed velocity that is used for departing the initial halo orbit, and ΔV_{A} the perturbed velocity that is used for entering into the target halo orbit.

When considering fuel consumption and flying time simultaneously, the objective function is chosen as

$$J(\boldsymbol{Z}) = \Delta V_{\mathrm{D}} + \|\Delta \boldsymbol{v}_{\mathrm{D}}\| + \|\Delta \boldsymbol{v}_{\mathrm{A}}\| + \Delta V_{\mathrm{A}} + \beta(t_{\mathrm{D}} + t_{\mathrm{I}} + t_{\mathrm{A}}) \tag{13}$$

where t_{D} is the time of the escape segment, t_{A} the time of the capture segment, and $\beta > 0$ the penalty factor.

The transfer trajectory must satisfy the terminal constraints

$$\boldsymbol{\Phi}_1(\boldsymbol{Z}) = \begin{bmatrix} \boldsymbol{\rho}(t_0) - \boldsymbol{X}_{\mathrm{D}}(\tau_{\mathrm{D}}, t_0) \\ \boldsymbol{\rho}(t_{\mathrm{f}}) - \boldsymbol{X}_{\mathrm{A}}(\tau_{\mathrm{A}}, t_{\mathrm{f}}) \end{bmatrix} = \boldsymbol{0} \tag{14}$$

where $t_{\mathrm{f}} = t_0 + t_{\mathrm{D}} + t_{\mathrm{I}} + t_{\mathrm{A}}$, $\boldsymbol{\rho}$ is the states of the spacecraft, and $\boldsymbol{X}_{\mathrm{D}}$ and $\boldsymbol{X}_{\mathrm{A}}$ are the states on the initial and target halo orbits, respectively.

In addition, the escape and capture points should be periapsides; thus, the following interior point constraints should be satisfied:

$$\boldsymbol{\Phi}_2(\boldsymbol{Z}) = \begin{bmatrix} \boldsymbol{\xi}_{\mathrm{D}}^{\mathrm{T}}(t_{\mathrm{PD}})\dot{\boldsymbol{\xi}}_{\mathrm{D}}(t_{\mathrm{PD}}) \\ \boldsymbol{\xi}_{\mathrm{A}}^{\mathrm{T}}(t_{\mathrm{PA}})\dot{\boldsymbol{\xi}}_{\mathrm{A}}(t_{\mathrm{PA}}) \end{bmatrix} = \boldsymbol{0} \tag{15}$$

$$\boldsymbol{\Phi}_3(\boldsymbol{Z}) = \begin{bmatrix} \dot{\boldsymbol{\xi}}_{\mathrm{D}}^{\mathrm{T}}(t_{\mathrm{PD}})\dot{\boldsymbol{\xi}}_{\mathrm{D}}(t_{\mathrm{PD}}) + \boldsymbol{\xi}_{\mathrm{D}}^{\mathrm{T}}(t_{\mathrm{PD}})\ddot{\boldsymbol{\xi}}_{\mathrm{D}}(t_{\mathrm{PD}}) \\ \dot{\boldsymbol{\xi}}_{\mathrm{A}}^{\mathrm{T}}(t_{\mathrm{PA}})\dot{\boldsymbol{\xi}}_{\mathrm{A}}(t_{\mathrm{PA}}) + \boldsymbol{\xi}_{\mathrm{A}}^{\mathrm{T}}(t_{\mathrm{PA}})\ddot{\boldsymbol{\xi}}_{\mathrm{A}}(t_{\mathrm{PA}}) \end{bmatrix} \geqslant \boldsymbol{0} \tag{16}$$

where $\boldsymbol{\xi}_{\mathrm{D}}$ and $\boldsymbol{\xi}_{\mathrm{A}}$ are the position vectors that are related to the escape and capture planets, $t_{\mathrm{PD}} = t_0 + t_{\mathrm{D}}$, and $t_{\mathrm{PA}} = t_{\mathrm{PD}} + t_{\mathrm{I}}$.

The multi-point boundary value problem that is expressed by Eqs. (12)–(16) can be solved by many methods. However, because the trajectory goes through several gravitational fields, the dynamic nonlinearity is very strong and the orbital constraints are quite sensitive to the variables. Therefore, the astringency of the numerical optimization method is very weak without initial guesses. To obtain good initial guesses, a trajectory searching method based on patched-models is proposed. As discussed above, the trajectory is composed of five segments whose orbital characteristics are quite different. According to the flying time and the stress on the spacecraft, the segments are investigated under different dynamic models: the unstable and stable segments are under a circular restricted three-body model, the escape and capture segments are under two-body models that are centered on the planets whose time is ignored, and the interplanetary segment is under a heliocentric two-body model. It should be noted that ephemeris constraints are considered here.

Based on the material above, the searching method can be described as follows:

Step 1 Under the heliocentric two-body model, the interplanetary segment is calculated using Lambert algorithms point-by-point within given time bounds. For each point, we obtain the moment t_{D} when the spacecraft reaches the influence sphere boundary of the initial planet, the escape hyperbolic excess velocity $\boldsymbol{v}_{\mathrm{D}}^{\infty}$, the time for the interplanetary segment t_{I}, and the capture hyperbolic excess velocity $\boldsymbol{v}_{\mathrm{A}}^{\infty}$.

Step 2 Under the CRTBP model, the first periapsides of the unstable and stable invariant manifolds are obtained.

Step 3 Under the two-body model centered on the planet, the velocity increments $\Delta \boldsymbol{v}_{\mathrm{D}}$ and $\Delta \boldsymbol{v}_{\mathrm{A}}$ are calculated to match the hyperbolic velocities $\boldsymbol{v}_{\mathrm{D}}^{\infty}$ and $\boldsymbol{v}_{\mathrm{A}}^{\infty}$ for every periapsis; then, for the parameters of the interplanetary segment, namely $t_{\mathrm{D}}, \boldsymbol{v}_{\mathrm{D}}^{\infty}, t_{\mathrm{I}}$, and $\boldsymbol{v}_{\mathrm{A}}^{\infty}$, the values that correspond to the minimum $\psi = \|\Delta \boldsymbol{v}_{\mathrm{D}}\| + \|\Delta \boldsymbol{v}_{\mathrm{A}}\|$ are obtained.

Step 4 Under the CRTBP model, the first periapsides of the unstable and stable pseudo-manifolds with various perturbed velocities ΔV are obtained.

Step 5 Under the two-body model centered on the planet, the periapsides obtained in Step 4 are transformed into an inertial frame, and the velocity increments $\Delta \boldsymbol{v}_{\mathrm{D}}$ and $\Delta \boldsymbol{v}_{\mathrm{A}}$ are calculated to match the hyperbolic velocities obtained in Step 3; the parameters of the best escape and capture trajectories $t_0, \tau_{\mathrm{D}}, \Delta V_{\mathrm{D}}, \Delta V_{\mathrm{A}}$, and τ_{A} are obtained with Eq. (13).

In this searching method, the whole trajectory is divided into several segments in such a way that the key parameters of each segment can be searched under a simple dynamics model.

4.2. Trajectories matching

The key procedure, which is expressed in the design steps, is to calculate the velocity increment at the periapsis. Taking the escape segment for an example as shown in Fig. 10, the two-point boundary value problem can be described as follows: for a given state of spacecraft expressed by $\boldsymbol{r}_1$ and $\boldsymbol{v}_1$, find an appropriate velocity increment $\Delta \boldsymbol{v}$ with which the spacecraft can reach the requested hyperbolic excess velocity $\boldsymbol{v}^{\infty}$. In this

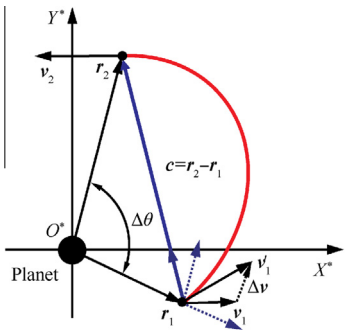

Fig. 10 Schematic diagram of a conic curve orbit.

section, an analytical algorithm is developed to solve this problem.

To calculate the velocity increment, the non-orthogonal coordinate is defined at the terminal points as follows: one axis directs the direction of the terminal position vector, and the other axis is along the ligature $\boldsymbol{c}$ of the two terminal points.[20] When the intersection angle $\Delta\theta$ between the position vectors $\boldsymbol{r}_1$ and $\boldsymbol{r}_2$ is not equal to π, the components of the terminal velocity vectors are

$$\begin{cases} v_{\mathrm{r}} = \sqrt{-\dfrac{g_{\mathrm{P}}}{4a}}(\coth\beta - \coth\alpha) \\ v_{\mathrm{c}} = \sqrt{-\dfrac{g_{\mathrm{P}}}{4a}}(\coth\beta + \coth\alpha) \end{cases} \tag{17}$$

where v_{r} is the velocity component on the radial direction, v_{c} the velocity component on the ligature direction, g_{P} the gravitational constant of the center planet, and a the semi-major axis of the conic curve. The instrumental variables α and β can be written as

$$\begin{cases} \sinh^2\alpha = -\dfrac{\|\boldsymbol{r}_1\| + \|\boldsymbol{r}_2\| + \|\boldsymbol{c}\|}{4a} \\ \sinh^2\beta = -\dfrac{\|\boldsymbol{r}_1\| + \|\boldsymbol{r}_2\| - \|\boldsymbol{c}\|}{4a} \end{cases} \tag{18}$$

It is known that $\beta > 0$ when $\Delta\theta < \pi$ and $\beta < 0$ when $\Delta\theta > \pi$, and the relation $\alpha \geqslant 0$ always exists. In the hyperbolic orbit, when $\|\boldsymbol{r}_2\| \to \infty$, Eq. (18) can be rewritten as

$$\begin{cases} \sinh^2\alpha = \lim\limits_{\|\boldsymbol{r}_2\|\to\infty}\left(-\dfrac{\|\boldsymbol{r}_1\| + \|\boldsymbol{r}_2\| + \|\boldsymbol{c}\|}{4a}\right) = +\infty \\ \sinh^2\beta = \lim\limits_{\|\boldsymbol{r}_2\|\to\infty}\left[-\dfrac{2\|\boldsymbol{r}_1\|\|\boldsymbol{r}_2\| + 2\|\boldsymbol{r}_1\|\|\boldsymbol{r}_2\|\cos\Delta\theta}{4a(\|\boldsymbol{r}_1\| + \|\boldsymbol{r}_2\| + \|\boldsymbol{c}\|)}\right] = -\dfrac{\|\boldsymbol{r}_1\|(1+\cos\Delta\theta)}{4a} \end{cases} \tag{19}$$

According to Eq. (19), the following relations can be obtained:

$$\coth\alpha = \frac{\sinh\alpha}{\cosh\alpha} = 1 \tag{20}$$

$$\coth\beta = \begin{cases} \sqrt{1 - \frac{4a}{\|\boldsymbol{r}_1\|(1+\cos\Delta\theta)}}, & \Delta\theta < \pi \\ -\sqrt{1 - \frac{4a}{\|\boldsymbol{r}_1\|(1+\cos\Delta\theta)}}, & \Delta\theta > \pi \end{cases} \tag{21}$$

In addition, the directions of the ligature $\boldsymbol{c}$ and $\boldsymbol{v}^\infty$ are almost the same. Using the relation $\sqrt{-g_{\mathrm{P}}/(4a)} = \|\boldsymbol{v}^\infty\|/2$ and Eqs. (20) and (21), the velocity after the execution of the escape velocity increment can be calculated by

$$\boldsymbol{v}_1' = \begin{cases} \left(\sqrt{\frac{G}{4}+H} + \frac{\|\boldsymbol{v}^\infty\|}{2}\right)\frac{\boldsymbol{v}^\infty}{\|\boldsymbol{v}^\infty\|} + \left(\sqrt{\frac{G}{4}+H} - \frac{\|\boldsymbol{v}^\infty\|}{2}\right)\frac{\boldsymbol{r}_1}{\|\boldsymbol{r}_1\|}, & \Delta\theta < \pi \\ \left(-\sqrt{\frac{G}{4}+H} + \frac{\|\boldsymbol{v}^\infty\|}{2}\right)\frac{\boldsymbol{v}^\infty}{\|\boldsymbol{v}^\infty\|} - \left(\sqrt{\frac{G}{4}+H} + \frac{\|\boldsymbol{v}^\infty\|}{2}\right)\frac{\boldsymbol{r}_1}{\|\boldsymbol{r}_1\|}, & \Delta\theta > \pi \end{cases} \tag{22}$$

where $G = (\|\boldsymbol{v}^\infty\|)^2$ and $H = g_{\mathrm{P}}/[\|\boldsymbol{r}_1\|(1+\cos\Delta\theta)]$.

For the condition where $\Delta\theta = \pi$, the semi-latus rectum of the hyperbolic orbit can be expressed by

$$p = \|\boldsymbol{r}_1\|(1 + e\cos\theta_1) = \|\boldsymbol{r}_2\|(1 - e\cos\theta_1) \tag{23}$$

where e is the orbital eccentricity, θ_1 the true anomaly at $\boldsymbol{r}_1$, and θ_2 the true anomaly at $\boldsymbol{r}_2$.

When $\Delta\theta = \pi$, Eq. (22) can be written as

$$p = \frac{2\|\boldsymbol{r}_1\|\|\boldsymbol{r}_2\|}{\|\boldsymbol{r}_1\| + \|\boldsymbol{r}_2\|} = \frac{2\|\boldsymbol{r}_1\|\|\boldsymbol{r}_2\|}{\|\boldsymbol{c}\|} \tag{24}$$

Then, the radial component of $\boldsymbol{v}_1'$ is

$$v_{\mathrm{r}} = \frac{he}{p}\sin\theta_1 = \frac{he}{p}\sin\theta_2 = -\|\boldsymbol{v}^\infty\| \tag{25}$$

where h is the value of the angular momentum.

The component of $\boldsymbol{v}_1'$ in the direction that is perpendicular to the radial vector is

$$v_\varphi = \frac{\sqrt{g_{\mathrm{P}}p}}{\|\boldsymbol{r}_1\|} = \sqrt{\frac{2g_{\mathrm{P}}}{\|\boldsymbol{r}_1\|}} \tag{26}$$

The value of $\boldsymbol{v}_1'$ is obtained as the components are determined. However, the direction of $\boldsymbol{v}_1'$ is unknown because there are countless vectors that are perpendicular to the radial vector. It is known that the minimum velocity increment can be found when the primary velocity $\boldsymbol{v}_1$ is on the same plane as the velocity $\boldsymbol{v}_1'$. Thus, when $\Delta\theta = \pi$, the optimal $\boldsymbol{v}_1'$ that is used for escaping is

$$\boldsymbol{v}_1' = \boldsymbol{v}^\infty + \sqrt{\frac{2g_{\mathrm{P}}}{\|\boldsymbol{r}_1\|}}\frac{(\boldsymbol{r}_1 \times \boldsymbol{v}_1) \times \boldsymbol{r}_1}{\|(\boldsymbol{r}_1 \times \boldsymbol{v}_1) \times \boldsymbol{r}\|} \tag{27}$$

With Eqs. (22) and (27), the velocity increment should be performed at the periapsis of the pseudo-manifold and can be calculated by

$$\Delta\boldsymbol{v} = \boldsymbol{v}_1' - \boldsymbol{v}_1 \tag{28}$$

5. Numerical simulation and analysis

Earth–Mars and Earth–Venus halo-to-halo transfer trajectories are chosen as simulation examples to demonstrate the proposed approach. In the Earth–Mars halo-to-halo transfer, the Sun–Earth L_1 halo orbit and the Sun–Mars L_2 halo orbit are chosen as the initial and target orbits, respectively. In the Earth–Venus halo-to-halo transfer, the Sun–Earth L_2 halo orbit and the Sun-Venus L_1 halo orbit are chosen as the initial and target orbits, respectively.

5.1. Earth–Mars halo-to-halo transfer

In this simulation example, the initial orbit is the Sun–Earth L_1 northern halo orbit, which has an amplitude that is equal to 1.6×10^5 km, and the target orbit is the Sun–Mars L_2 northern halo orbit, which has an amplitude that is equal to 1.2×10^5 km. The range of the launch time is 2018-01-01 to 2018-12-31, and the maximum allowable flying time is 500 days. By employing the proposed search method, the contour of the total velocity increment is used for completing the Earth–Mars halo-to-halo transfer, employing the traditional invariant manifold; this scenario is shown in Fig. 11. The transfer trajectory of the optimal solution is shown in Fig. 12.

It can be found from Fig. 11 that the solution space is separated into two parts in which the local minimum solution is lower in the upper half part. The optimal solution whose total velocity increment is approximately 2.72 km/s can be found. For this solution, the Earth escape time is 2018-04-21, the flying time of the interplanetary segment is 257.58 days, the

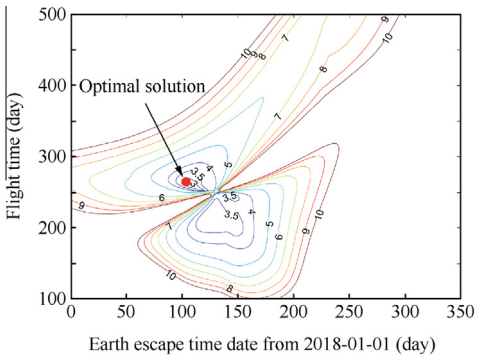

Fig. 11 Contour of the total velocity increment that is used for completing the Earth–Mars halo-to-halo transfer.

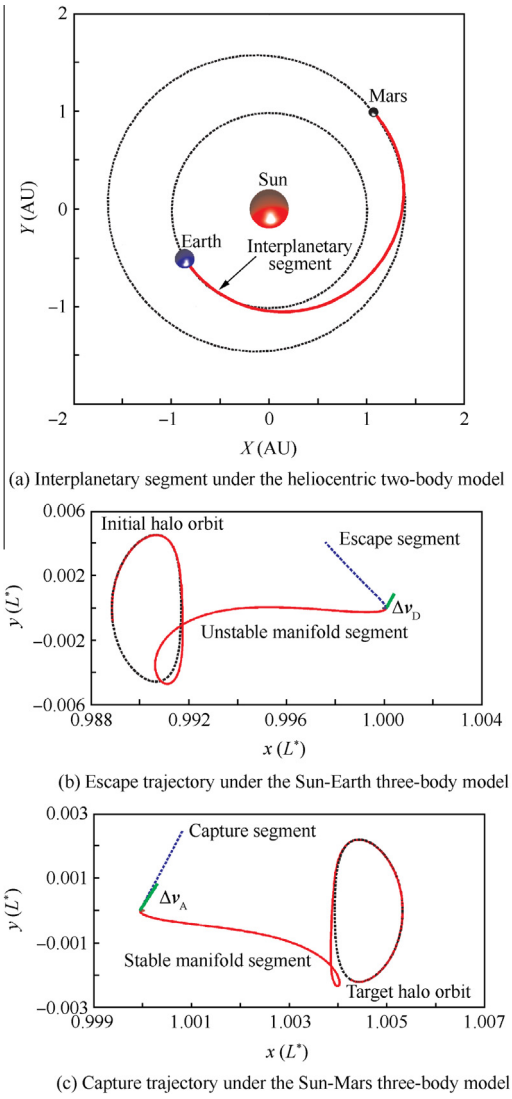

Fig. 12 Earth–Mars halo-to-halo transfer trajectory that employs an invariant manifold and planetary gravity assist.

escape hyperbolic excess velocity is $\boldsymbol{v}_{\mathrm{D}}^{\infty} = [2.86 \ -1.37 \ 0.56]^{\mathrm{T}}$ km/s, and the capture hyperbolic excess velocity is $\boldsymbol{v}_{\mathrm{A}}^{\infty} = [0.57 \ -3.37 \ -1.18]^{\mathrm{T}}$ km/s. Fig. 12 shows that the escape and capture segments are hyperbolic curves under the three-body model. This is because the time of the two segments is so short that the influence of Sun can be neglected.

For the transfer opportunity that is obtained by employing the orbit matching method, the influence of parameters τ and ΔV on the velocity increment and the flying time of the manifold segments are drawn in Figs. 13–16. In these figures, EPM and MPM denote the solution trajectories that employ the pseudo-manifolds around Earth and Mars, respectively; the sum of ΔV_{D} and $\|\Delta \boldsymbol{v}_{\mathrm{D}}\|$ is defined as the escape velocity increment, and the sum of $\|\Delta \boldsymbol{v}_{\mathrm{A}}\|$ and ΔV_{A} is defined as the capture velocity increment.

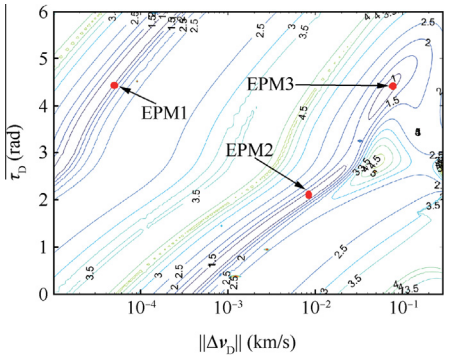

Fig. 13 Contour of the escape velocity increment.

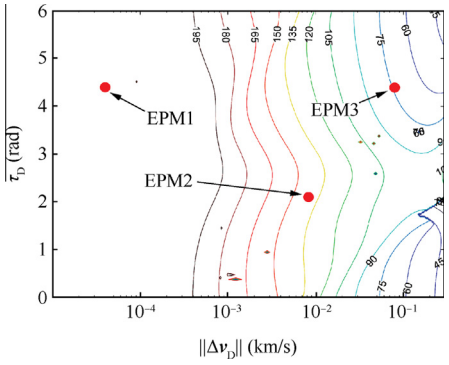

Fig. 14 Flying time of the unstable manifold segment.

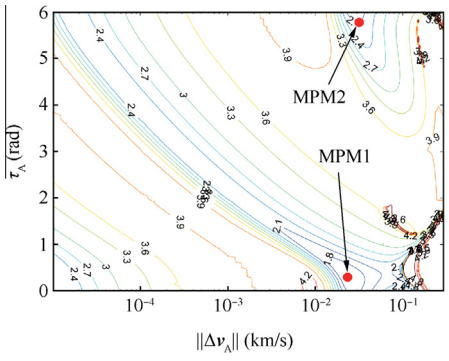

Fig. 15 Contour of the capture velocity increment.

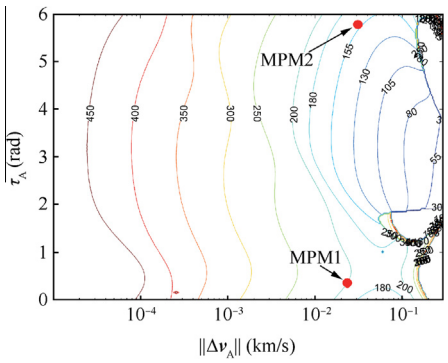

Fig. 16 Flying time of the stable manifold segment.

Figs. 13 and 14 represent that there are several local extremums of the velocity increment, and the flying time reduces as the perturbed velocity ΔV increases. The appropriate solutions can be obtained by accounting for the velocity increment and the flying time simultaneously. As Fig. 13 shows, three local minimum solutions, which are called EPM1, EPM2, and EPM3, can be found. According to Fig. 14, EPM1 can be eliminated due to having a flying time that is too long; EPM2 has the minimum velocity increment, and its flying time is 140 days; EPM3 cost only 74 days, although its velocity increment is slightly larger than that of EPM2. EPM2 and EPM3 can both be chosen as an appropriate escape trajectory. The detailed variables are shown in Table 1.

As shown in Figs. 15 and 16, there are two local minimum values for the capture velocity increment, and the flying time reduces as the perturbed velocity ΔV increases. The two local minimum values are not very different with respect to the velocity increment and the flying time. Therefore, both of the two solutions can be chosen as appropriate capture trajectories. The design results are listed in Table 1.

In Table 1, EIM and MIM denote the solution trajectories that employ the invariant manifolds around Earth and Mars, respectively, and t_d and t_a are the times of the unstable and stable manifold segments, respectively. EPM not only has much less flying time but also has a lower escape velocity increment compared to EIM. The reason for this phenomenon is that the perturbed velocity expends the distribution of the periapsides. Additionally, MPM1 and MPM2 can save more flying time and velocity increments compared to MIM. These results verify the advantage of employing a pseudo-manifold to construct a fast low-energy transfer trajectory. A comparison of the results obtained from the proposed approach and previous studies is shown in Table 2 where Δv_{sum} is the total velocity used for trasfer.

Table 2 Comparison of Earth–Mars transfer trajectories.

Approach	t_0 (yyyy-mm-dd)	Δt (day)	Δv_{sum} (km/s)
Ref. [9]	—	2919	5.28
Ref. [8]	2017-01-19	1699	4.25
Ref. [10]	2019-09-21	910	3.97
Proposed	2017-12-01	596	2.06

It can be seen from Table 2 that the transfer can achieve significant fuel consumption savings by introducing the planetary gravity assist. At the same time, the flying time is reduced effectively by replacing the invariant manifold with a pseudo-manifold.

5.2. Earth–Venus halo-to-halo transfer

In this simulation example, the initial orbit is the Sun–Earth L_2 northern halo orbit with an amplitude equal to 1.6×10^5 km, and the target orbit is the Sun–Venus L_1 halo orbit with an amplitude equal to 2.0×10^5 km. The range of the launch time is 2013-01-01 to 2014-12-31, and the maximum flying time is 300 days. The results obtained by the proposed method are listed in Table 3.

In Table 3, VIM denotes the solution trajectory that employs the invariant manifold, VPM denotes the solution trajectory that employs the pseudo-manifold. EPM1 has almost the same velocity increment as EIM but has 62.08 days shorter flying time. Compared to EIM, EPM can save 141.31 days, although it has a slightly larger velocity increment. Compared to VIM, VPM1 can save a 0.92 km/s velocity increment and 109.01 days of flying time, and VPM2 can save a 0.85 km/s velocity increment and 109.81 days of flying time. Again, the advantage of employing a pseudo-manifold to construct a fast low-energy transfer trajectory is verified.

The transfer trajectories with minimum fuel consumption in each launch window between the years 2013 and 2018 are listed in Table 4, where Δt indicates the total flying time. The flying times are approximately 140–160 days shorter than those of the solution trajectories that employ the traditional invariant manifold.

Table 1 Parameters of the Earth–Mars halo-to-halo transfer.

Parameters of the escape trajectory				
Type	τ_D (rad)	ΔV_D (km/s)	t_d (day)	$\|\Delta \boldsymbol{v}_D\|$ (km/s)
EIM	6.0937	—	384.0345	0.5822
EPM2	2.0839	0.0084	140.1897	0.5561
EPM3	4.4173	0.0781	73.9638	0.7547
Parameters of the capture trajectory				
Type	τ_A (rad)	ΔV_A (km/s)	t_a (day)	$\|\Delta \boldsymbol{v}_A\|$ (km/s)
MIM	5.0202	—	451.3422	2.1345
MPM1	0.3157	0.0235	198.7760	1.4725
MPM2	6.0489	0.0311	175.3638	1.8866

Table 3 Parameters of the Earth–Venus halo-to-halo transfer.

Parameters of the escape trajectory				
Type	τ_D (rad)	ΔV_D (km/s)	t_d (day)	$\|\Delta \boldsymbol{v}_D\|$ (km/s)
EIM	3.3784	—	205.9834	0.6653
EPM1	5.9359	0.0145	133.9083	0.6346
EPM2	2.0059	0.1024	64.6739	0.8524
Parameters of the capture trajectory				
Type	τ_A (rad)	ΔV_A (km/s)	t_a (day)	$\|\Delta \boldsymbol{v}_A\|$ (km/s)
VIM	3.7573	—	172.2753	2.8179
VPM1	3.6941	0.1150	63.2663	1.7824
VPM2	3.6728	0.1675	62.4647	1.8034

Table 4 Earth–Venus halo-to-halo transfer trajectories with minimum fuel consumption.

t_0 (yyyy-mm-dd)	ΔV_D (km/s)	$\|\Delta \boldsymbol{v}_D\|$ (km/s)	$\|\Delta \boldsymbol{v}_A\|$ (km/s)	ΔV_A (km/s)	Δv_{sum} (km/s)	Δt (day)
2013-06-10	0.0145	0.6346	1.7824	0.1150	2.5465	363.3362
2015-01-14	0.0098	1.0443	0.6003	0.0051	1.6595	381.4387
2016-08-26	0.0505	2.2977	0.6672	0.0055	3.0209	379.3160
2018-02-15	0.0190	0.6626	2.7205	0.0089	3.4110	372.1476

6. Conclusions

(1) The manifold and the planetary gravity assist are combined to construct the transfer in such a way that fuel consumption can be saved significantly.
(2) The pseudo-manifold is employed to take the place of the traditional invariant manifold; as a result, the flying time is reduced obviously, and more transfer opportunities are obtained.
(3) A searching method based on patched-models, which can be used for a rapid global search, is proposed to provide initial fast low-energy transfers.
(4) The numerical simulation results indicate that significant fuel consumption and flying time savings can be achieved by the proposed approach.

Acknowledgments

The authors thank the anonymous reviewers for their critical and constructive review of the manuscript. This study was co-supported by the National Basic Research Program of China (No. 2012CB720000) and the National Natural Science Foundation of China (No. 11102021).

References

1. Belló M, Gómez G, Masdemont JJ. Invariant manifolds, Lagrangian trajectories and space mission design. In: Perozzi E, Ferraz-Mello S, editors. *Space manifold dynamics*. New York: Springer Science + Business Media, LLC; 2010. p. 1–96.
2. Farquhar RW, Dunham DW, Guo YP, McAdams JV. Utilization of libration points for human exploration in the Sun–Earth–Moon system and beyond. *Acta Astron* 2004;**55**(3-9):687–700.
3. Farquhar RW, Muhonen DP, Richardson DL. Mission design for a halo orbiter of the Earth. *J Spacecraft Rockets* 1977;**14**(3):170–7.
4. Dunham DW, Farquhar RW. Libration point missions, 1978–2002. In: Gómez G, Lo MW, Masdemont JJ, editors. *Libration point orbits and applications*. Girona, Spain: World Scientific Publishing Company; 2002. p. 45–73.
5. Kwong J, Norris SD, Hopkins JB, Buxton CJ, Pratt WD, Jones MR. Stepping stones: exploring a series of increasingly challenging destinations on the way to Mars. 2011; Report No.: AIAA-2011-7216.
6. Zimmer AK. Investigation of vehicle reusability for human exploration of Near-Earth asteroids using Sun–Earth libration point orbits. *Acta Astron* 2013;**90**(1):119–28.
7. Pergola P, Geurts K, Casaregola C, Andrenucci M. Earth–Mars halo to halo low thrust manifold transfers. *Celest Mech Dyn Astr* 2009;**105**(1):19–32.
8. Wang YM, Cui PY, Qiao D. Opportunities search of transfer between interplanetary halo orbits in ephemeris model. *Sci China Ser E Tech Sci* 2013;**56**(1):188–93.
9. Alonso GP. The design of system-to-system transfer arcs using invariant manifolds in the multi-body problem [dissertation]. West Lafayette (IN): Purdue University; 2006.
10. Topputo F, Vasile M, Bernelli-Zazzera F. Low-energy interplanetary transfers exploiting invariant manifolds of the restricted three-body problem. *J Astronaut Sci* 2005;**53**(4):353–72.
11. Hou XY, Liu L, Zhao YH. On some applications of invariant manifolds. *Res Astron Astrophys* 2011;**11**(1):103–18.
12. Nakamiya M, Yamakawa H, Scheeres DJ, Yoshikawa M. Interplanetary transfers between halo orbits: connectivity between escape and capture trajectories. *J Guid Control Dyn* 2010;**33**(3):803–13.
13. Szebehely VG. *Theory of orbits in the restricted problem of three bodies*. New York: Academic Press; 1967. p. 16–22.
14. Xu M. Overview of orbital dynamics and control for libration point orbits. *J Astronaut* 2009;**30**(4):1299–313 [Chinese].
15. Li MT. Low-energy trajectory design and optimization for collinear libration points missions [dissertation]. Beijing: Graduate School, Chinese Academy of Sciences; 2010 [Chinese].
16. Lantoine G, Russell RP. Near ballistic halo-to-halo transfers between planetary moons. *J Astronaut Sci* 2011;**58**(3):335–63.
17. Ren Y. Design and optimization of low-thrust interplanetary transfer trajectory [dissertation]. Harbin: School of Astronautics, Harbin Institute of Technology; 2007 [Chinese].
18. Davis K, Born G, Butcher E. Transfers to earth-moon L_3 halo orbits. *Acta Astron* 2013;**88**:116–28.

19. Davis DC, Howell KC. Characterization of trajectories near the smaller primary in restricted problem for applications. *J Guid Control Dyn* 2012;**35**(1):116–28.
20. Godal T. Conditions of compatibility of terminal positions and velocities*Proceedings of the Eleventh International Astronautical Congress*. Stockholm, Sweden: Springer-Verlag; 1960.

Shang Haibin is an associate professor in the School of Aerospace Engineering at Beijing Institute of Technology, Beijing, China. He received his Ph.D. degree from Harbin Institute of Technology in 2008. His main research interests include astrodynamics, spacecraft dynamics and control, orbit design and optimization.

Wang Shuai is a Ph.D. student at Beijing Institute of Technology. His area of research includes spacecraft dynamics and control, orbit design and optimization.

Cui Pingyuan is a professor and Ph.D. advisor in the School of Aerospace Engineering at Beijing Institute of Technology, Beijing, China. He received his Ph.D. degree from Harbin Institute of Technology in 1990. His current research interests are flight dynamics and control, spacecraft dynamics and control, orbit design and optimization.